Received: 23 March 2021 | Revised: 17 September 2021 | Accepted: 20 September 2021

DOI: 10.1002/mrm.29041

RESEARCH ARTICLE

Magnetic Resonance in Medicine

Off-resonance saturation as an MRI method to quantify mineral- iron in the post-mortem brain

Lucia Bossoni[1] | **Ingrid Hegeman-Kleinn**[2] | **Sjoerd G. van Duinen**[2] | **Marjolein Bulk**[1,3] | **Lena H. P. Vroegindeweij**[4] | **Janneke G. Langendonk**[4] | **Lydiane Hirschler**[1] | **Andrew Webb**[1] | **Louise van der Weerd**[1,5]

[1]C. J. Gorter Center for High field MRI, Department of Radiology, Leiden University Medical Center, Leiden, The Netherlands

[2]Department of Pathology, Leiden University Medical Center, Leiden, The Netherlands

[3]Department of Neurology, Alzheimer Center, Erasmus University Medical Center, Rotterdam, The Netherlands

[4]Department of Internal Medicine, Center for Lysosomal and Metabolic Diseases, Porphyria Center Rotterdam, Erasmus University Medical Center, Rotterdam, The Netherlands

[5]Department of Human Genetics, Leiden University Medical Center, Leiden, The Netherlands

Correspondence
Lucia Bossoni, C. J. Gorter Center for High field MRI, Department of Radiology, Leiden University Medical Center, PO Box 9600, 2300 RC Leiden, The Netherlands.
Email: l.bossoni@lumc.nl

Funding information
This study was supported by the Netherlands Organization for Scientific Research (NWO) through a VENI fellowship to L.B. (0.16.Veni.188.040)

Purpose: To employ an off-resonance saturation method to measure the mineral-iron pool in the postmortem brain, which is an endogenous contrast agent that can give information on cellular iron status.

Methods: An off-resonance saturation acquisition protocol was implemented on a 7 Tesla preclinical scanner, and the contrast maps were fitted to an established analytical model. The method was validated by correlation and Bland-Altman analysis on a ferritin-containing phantom. Mineral-iron maps were obtained from postmortem tissue of patients with neurological diseases characterized by brain iron accumulation, that is, Alzheimer disease, Huntington disease, and aceruloplasminemia, and validated with histology. Transverse relaxation rate and magnetic susceptibility values were used for comparison.

Results: In postmortem tissue, the mineral-iron contrast colocalizes with histological iron staining in all the cases. Iron concentrations obtained via the off-resonance saturation method are in agreement with literature.

Conclusions: Off-resonance saturation is an effective way to detect iron in gray matter structures and partially mitigate for the presence of myelin. If a reference region with little iron is available in the tissue, the method can produce quantitative iron maps. This method is applicable in the study of diseases characterized by brain iron accumulation and can complement existing iron-sensitive parametric methods.

KEYWORDS
ferritin, iron, neurodegenerative diseases, postmortem MRI

1 | INTRODUCTION

Physiological iron is distributed heterogeneously within the brain, with the structures richest in iron being localized within the basal ganglia.[1] The distribution of iron throughout the brain is likely related to its fundamental biological processes, which involve oxygen transport, DNA synthesis, and mitochondrial respiration.[2] In contrast, the dysregulation of iron homeostasis is associated with neurotoxicity via the formation of reactive oxygen species,[2–6] lipid peroxidation,[7] and ferroptosis,[8] a form of cell death characterized by phospholipid oxidation.[9] Iron is also thought to trigger inflammation which can, in turn, lead to additional cellular iron release.[10]

Brain iron accumulation is a common phenomenon of several neurodegenerative diseases despite their different pathological hallmarks. Examples are Alzheimer disease (AD),[2,11] Huntington disease (HD),[2,4,12] and the neurodegeneration with brain iron accumulation group of disorders, of which aceruloplasminemia (ACP) is a rare phenotype.[13]

One of the primary cytoplasmic proteins responsible for intra- and extracellular iron storage is ferritin.[14] Ferritin is composed of a 24-subunit shell (apoferritin), which plays 3 important roles in iron regulation: it binds cytoplasmic Fe^{2+}, oxidizes Fe^{2+} into Fe^{3+} (as antioxidant protection), and stores iron in the form of a biocompatible nanomineral[15]—ferrihydrite—or a mixture of ferrihydrite and other minerals.[16,17] Because the core of ferritin can bind up to ~5000 iron atoms, the nanoparticle's saturated magnetic moment can reach ~300 μ_B.[18] Ferritin-iron levels constitute ~80% of total non-heme iron[19]; therefore, ferritin is commonly used as a reporter of tissue iron status. Although ferritin-iron is unlikely to contribute directly to oxidative stress, its levels are related to the labile iron pool,[20,21] which is implicated in neurotoxicity.

MRI is very sensitive to the magnetic field perturbation caused by iron ions and iron nanominerals, which have superparamagnetic properties. In the presence of iron, diffusing water molecules probe a broad distribution of magnetic fields. Consequently, a time-dependent phase is accumulated, leading to reduced T_2 and T_2^* relaxation times.[22–24] Ferritin-iron is the (physiological) iron form having the largest effect on the MRI signal,[19] thanks to its large susceptibility and abundance. The most sensitive MR methods for the detection of iron are the field-dependent transverse relaxation rate increase,[25–27] R_2^* and R_2 mapping,[28,29] and QSM.[30] Although quantitative maps of transverse relaxation rates and tissue magnetic susceptibility have already shown benefits in the clinic,[22,31] these parameters are also influenced by myelin content,[32–34] fiber orientation,[35] tissue microstructure,[36] neuronal loss[29] and iron aggregation.[37,38] Additionally, QSM reconstructions can be affected by the nonlocal nature of the inverse problem that relates magnetic field perturbation to magnetic susceptibility, and this impairs quantitative analysis.

In this work, we show how an off-resonance saturation (ORS) method, earlier introduced for the detection of iron-oxide contrast agents,[39,40] can be employed to assess mineral-iron levels in the postmortem brain and overcomes some of the limitations of conventional mapping methods.

We validated the method in a ferritin phantom, and we employed it to characterize the mineral-iron levels in postmortem material obtained from 5 patients affected by neurological diseases associated with increased brain iron. We assessed the accuracy of the mineral-iron maps to report on tissue iron status against QSM, R_2^* maps, and histopathological staining for ferric iron, ferritin, and myelin.

2 | METHODS

2.1 | Tissue selection and phantom preparation

A ferritin-agarose phantom was prepared by adding horse spleen ferritin (Sigma-Aldrich, St. Louis, Missouri, ref. F4503) to a 1.5% agarose solution. Phantoms with different iron concentrations were prepared: 0 mM, 1.3 mM, 4.0 mM, 7.0 mM, 10.3 mM, and 15.1 mM. The iron concentration was estimated by multiplying the ferritin concentration by the average loading of the protein, that is, 2500 iron/ferritin.[41]

Formalin-fixed tissue blocks extracted from 5 diseased brains were studied. Brain material from 3 patients with HD, 1 patient with AD, and 1 patient with ACP was obtained from the pathology department of the Leiden University Medical Center (Leiden, The Netherlands), the Netherlands Brain Bank (Amsterdam, The Netherlands), and the Erasmus Medical Center (Rotterdam, The Netherlands), respectively. Patient's informed consent was obtained from each respective brain bank. For each case, a disease-relevant area was chosen: the striatum for the HD case, the striatum and the globus pallidus for the ACP case, and the middle temporal gyrus for the AD case. The tissue blocks were rehydrated in phosphate-buffered solution for 24 hours prior to the MRI scan to partially restore T2s. Subsequently, the tissue was scanned in a hydrogen-free solution (Fomblin LC08, Solvay S. A., Brussels, Belgium).

2.2 | MRI data acquisition

MRI data were acquired on a 7 Tesla preclinical scanner (Bruker Biospin, Ettlingen, Germany) using a 38-mm linear birdcage transmit-receive coil (T10327V3) with 8 legs.

To compare the iron maps obtained with ORS to standard QSM and R_2^* maps, R_2^*-weighted images were acquired using a 3D multiple gradient echo (MGE) sequence. In the case of the ACP tissue, the TE and inter-TE were shortened (by doubling the receiver bandwidth) to increase SNR because the heavier iron load in this tissue severely shortened the transverse relaxation parameters. The acquisition parameters are summarized in Table 1.

ORS images were derived from 2D steady-state free precession images (Bruker fast imaging with steady-state precession-FID) with TE/TR = 3/6 ms; interscan delay TR = 2 s; flip angle = 10 degrees. A "control" magnitude image ($M_{control}$), without saturation pulses, was also acquired. The steady-state free precession acquisition module was chosen for convenience, given the high SNR per scan time that is delivered by the acquisition method. The steady state condition was not a necessary requirement. Saturated images (M_{sat}) were produced by a saturation module consisting of a train composed by the repetition of a hyperbolic secant pulse (bandwidth 500 Hz, duration 40.5 ms, B_1 = 1.36 μT, β-factor = 5), followed by a spoiler gradient of 3 ms of duration. The pulse-gradient unit was repeated 6 times with an interval of 5 ms in-between the gradients and the successive RF pulse. The off-resonance saturation pulses were phase-cycled to improve spoiling. A list of M_{sat} was obtained upon varying the frequency of the off-resonance pulse. Details of the off-resonance acquisition are reported in Table 2.

2.3 | MRI data processing

MGE-magnitude images were fitted on a pixel-by-pixel basis to a mono-exponential decay function,[23] after ruling out the presence of multi-components, using the Levenberg–Marquardt curve-fitting algorithm to derive the transverse relaxation rate R_2^*. In the case of the ACP tissue, the echoes with intensities laying in the noise level (SNR ≤ 1) were excluded from the fit.

Susceptibility values (χ) were calculated from the phase images with the STI-Suite Matlab (Natick, Massachusetts) toolbox (version 2.2). Phase unwrapping of the measured phase images and removal of the background field were done with iHARPERELLA,[42] whereas magnetic susceptibility calculation and streaking artifact correction were performed with the iLSQR algorithm.[43] Raw susceptibility values are reported because no reference region was available in these small tissue samples.

Figure 1 illustrates the pipeline of the ORS analysis. ORS images (M_{ors}) were obtained from the subtraction: $M_{ors} = M_{control} - M_{sat}$. Contrast (C) maps were obtained by subtracting the mean intensity of M_{ors} in a region of reference (ROR) from the M_{ors}.[40] Under the assumption that the ROR contains no iron, the contrast (C) can be written as the product of the fraction of protons (φ) saturated by the ORS pulses and the intensity of the control image ($C = M_{control}\,\varphi$). In our work, only positive frequency offsets were chosen to exclude nuclear Overhauser effects-related artifacts[44] and to speed up the acquisition. The saturated fraction of protons, as derived by Delangre et al.,[40] is given by:

$$\phi = \frac{1}{\pi}\left|\operatorname{arctg}\left(a\left(\Delta\nu_0 - \delta\nu + \frac{BW}{2}\right)\right) - \operatorname{arctg}\left(a\left(\Delta\nu_0 - \delta\nu - \frac{BW}{2}\right)\right)\right|, \quad (1)$$

where $a = \frac{3\sqrt{3}\nu_{mat}^{-1}}{2\pi\gamma[Fe]B_{eq}} = \frac{\alpha}{[Fe]B_{eq}}$, γ is expressed in MHz/T; $B_{eq} = \frac{\mu_0 M_s}{3}$ is the stray field (in Tesla) at the equator of a nanoparticle with saturation magnetization M_S; [Fe] is the iron concentration (in mM); ν_{mat} is the molar volume of ferrihydrite[45] and is equal to 5.4×10^{-6} $m^3/mol = 5.4 \times 10^{-6}$ mM^{-1}; and $\alpha = 3.6 \times 10^{-3}$ T $(Hz\ mM)^{-1}$ (see Supporting Information for further details). We added a frequency offset ($\delta\upsilon$) to account for resonance frequency shifts. Because N = 6 saturation pulses were used to enhance the saturation,[46] the final expression for the contrast becomes:

$$C\left(\Delta\nu_0\right) = NM_{control}\phi\left(\Delta\nu_0\right) + off. \quad (2)$$

$M_{control}$ is weighted by the proton density, relaxation times, and flip angle.[47] The offset (*off*) term in the equation above was introduced to account for residual MT effects and imperfect saturation. Finally, the contrast map was fitted to Equation (2) to derive the iron concentration, with the equatorial field as a fixed parameter. The agreement between the fitted iron concentration and the known iron concentration was assessed with correlative and Bland-Altman analyses.

TABLE 1 Summary of the acquisition parameters for the MGE sequence, with 8 echoes (N_{echo})

Sample	Pixel Size (mm^3)	FA (degrees)	Averages	TR (ms)	TE_1 (ms)	N_{echo}	ΔTE	Total Scan Time
HD	$(0.15)^3$	25	20	107.3	5.2	8	4.34	3 h 26 m
ACP	$(0.15)^3$	25	20	130.4	1.96	8	2.21	3 h 55 m
AD	$(0.15)^3$	25	20	107.3	5.2	8	4.34	3 h 26 m

Abbreviations: ΔTE interecho time; ACP, aceruloplasminemia; AD, Alzheimer disease; FA, flip angle; HD, Huntington disease; MGE, multiple gradient echo; TE_1, first echo time.

TABLE 2 Summary of the acquisition parameters for the ORS-SSFP acquisition

Sample	BW [Hz]	$\Delta\upsilon_0$ range [Hz]	υ_{int} [Hz]	Total Scan Time	Pixel Size (mm^3)	Reference for Contrast Calculation (ROR)
Phantom	500	250-649	7	1.3 h	$0.3 \times 0.3 \times 2$	Agarose-only compartment
HD	500	250-700	5	~8 h 10 min	$0.15 \times 0.15 \times 2$	Internal capsule
ACP	500	250-700	5	~8 h 10 min	$0.15 \times 0.15 \times 2$	Internal Capsule
AD	500	250-700	5	~8 h 10 min	$0.15 \times 0.15 \times 2$	Cortical white matter

Abbreviations: $\Delta\upsilon_0$, frequency of the off-resonance saturation pulse; υ_{int}, interval between ORS frequencies; BW, bandwidth; ORS-SSFP, off-resonance saturation–steady-state free precession; ROR, region of reference.

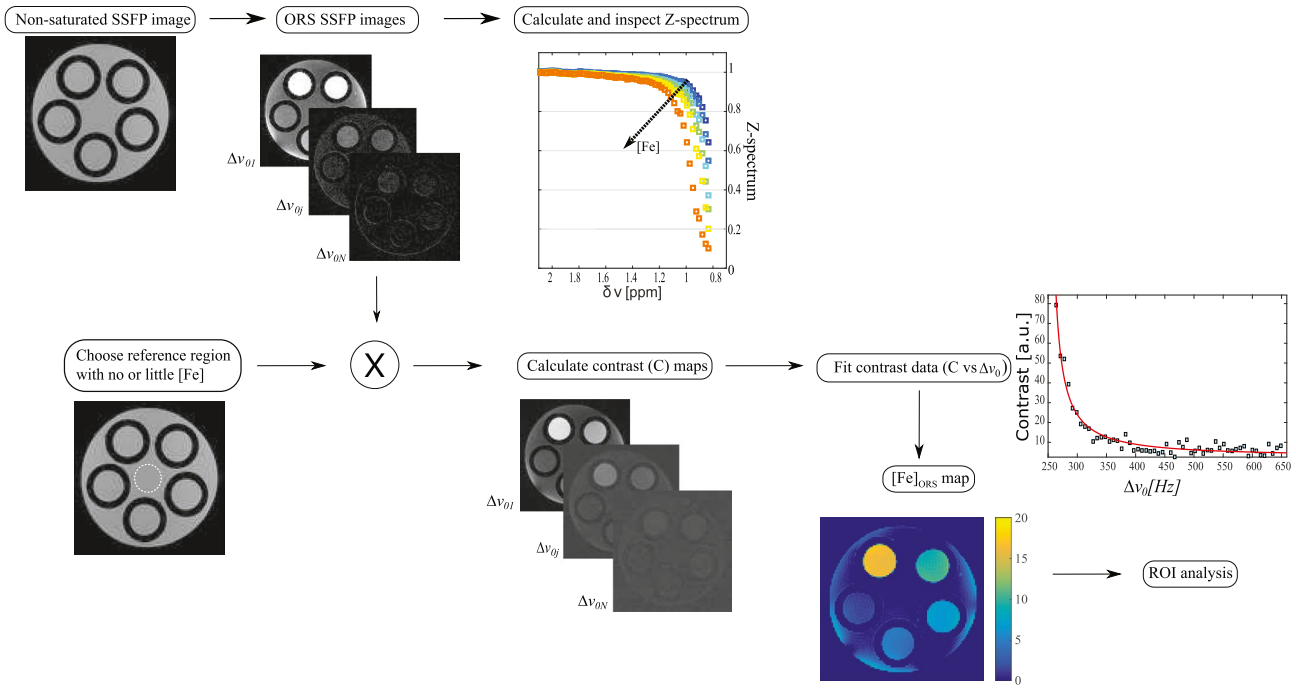

FIGURE 1 Analysis pipeline. After the acquisition of the nonsaturated images ("control"), the saturated images are acquired, and the ORS image is derived. The Z-spectrum is shown but was not used in the analysis. The ROR is shown here as a white dotted line in the bottom row. The contrast maps are obtained from the ORS image and the mean intensity in the ROR and fitted to the model discussed below. An example of the fit is shown in the right panel. The fit is the red solid line overlapped on to the experimental data (blue squares). Finally, a map of iron concentration in mM is obtained ($[Fe]_{ORS}$ map). ORS, off-resonance saturation; ROR, region of reference; SSFP, steady-state free precession

2.4 | Histopathological validation

The same tissue blocks used for MRI were employed for histology. Tissue blocks were embedded in paraffin and sliced with a microtome into 5 μm and 20 μm thick sections. The 20 μm sections were employed for non-heme iron detection (Meguro staining) according to Van Duijn et al.[48] After deparaffinization, the tissue sections were incubated for 80 min in 1% potassium ferro-cyanide and then washed, followed by 100 min incubation in methanol with 0.01 M NaN_3 and 0.3% H_2O_2. Subsequently, sections were washed with 0.1 M phosphate buffer, followed by 80 min incubation in a solution containing 0.025% 3'3-diaminob enzidine-tetrahydrochloride (Sigma-Aldrich) and 0.005% H_2O_2 in 0.1 M phosphate buffer. The reaction was stopped by washing with tap water. The 5 μm slices were used for additional staining: non-heme (mostly trivalent) iron was detected with Perl's Prussian blue (Merck 1.04984.0100, Darmstadt, Germany), and immunohistochemical detection of myelin was done with anti-myelin PLP antibody (Bio-Rad, MCA 839G, Hercules, California) with second antibody Rb-aMs/biotin (Dako, Santa Clara, California) for 1 h at room temperature, followed by avidin-biotin-complex (HRP, ABC Elite Kit, Vector Laboratories, Inc., Burlingame, California) for 30 min at room temperature. Immunohistochemical detection of ferritin was done with ferritin antibody (Bethyl A80-140, dilution 1:1000, overnight incubation at room temperature; Bethyl Laboratories,

Inc., Montgomery, Texas), with as a second step antigoat/biotin (Betyhl A50-204B, dilution:1:1000, 1 h incubation at room temperature), followed by ABC incubation for 30 min at room temperature. After the ABC treatment, the tissue was rinsed 3 times with phosphate-buffered saline and incubated in 0.05% 3'3-diaminobenzidine-tetrahydro chloride (Sigma-Aldrich) with 15 μl 30% H_2O_2/100 ml for 5-10 min. After rinsing several times with demineralized water, the slices were counterstained for 30 s with Harris hematoxylin and washed for 5-10 mins with tap water. Finally, the tissue sections were dehydrated with ethanol 70%, 96% , and 100%, as well as xylene.

2.5 | Correlation between histology and ORS imaging

To quantify the degree of agreement between the histological staining of iron with the mineral-iron concentration derived from the ORS method, oval regions of interest (ROI) (N = 30-40) were drawn in the gray and white matter regions (excluding the ROR) of all the MRI and histology images, except for the Perl's Prussian blue. The histological images were manually coregistered (affine transformation) to the MRI maps with the TrackEM2 plugin in ImageJ. The registered image stack was converted to an 8-bit grayscale image. Oval ROIs were carefully drawn and propagated among maps with the ROI manager tool. Mean gray values from the predefined ROIs were quantified[32] after inspecting for the precise placement of the ROIs. Pearson correlation coefficients (ρ) and *P* values were calculated per case with the *corrplot* package in R (R version 3.6.3). The Supporting Information shows the location where the ROIs where drawn (Supporting Information Figures S3, S9 and S10).

3 | RESULTS

3.1 | Validation on a ferritin phantom

Figure 2 shows the iron map obtained from the ferritin-loaded phantom and the ROI analysis on the sample's compartments. The ROR was drawn in the middle of the phantom containing only agarose (Figure 1). The best-fitting results were obtained when fixing $B_{eq} = 1$ mT, which is very close to the theoretical value for ferritin (see Supporting Information). The fitted iron concentration agrees well with the nominal iron concentration, as assessed by the correlative plot in Figure 2C. Furthermore, the agreement between the iron concentration, derived from the ORS map and the nominal iron concentrations, was assessed by Bland-Altman analysis (Figure 2D),[49,50] considering the latter parameter as the reference value. No data fell outside of the limits of agreement, and no systematic bias was detected at the 5% level of significance.

3.2 | Application to postmortem material

Figure 3 shows the results obtained from the middle temporal gyrus of the AD case. A comparison is shown between the MRI parametric maps, that is, R_2^*, QSM, and the ORS iron map (termed $[Fe]_{ORS}$ map in the rest of the article); and histology, that is, myelin, iron, and ferritin. Elevated R_2^* levels are seen in the myelin-rich white matter (white arrowheads in Figure 3) and in the cortex (white arrows in Figure 3). In the QSM map, negative susceptibility is predominantly detected in the white matter. The $[Fe]_{ORS}$ map shows the localization of the iron in the cortex and (partially) in the white matter, thus largely mirroring the QSM paramagnetic contrast and the histological staining of iron and ferritin (protein), whereas it appears poorly localized to areas of positive myelin staining. Across all tissue blocks, the Perl's staining was considerably weaker than the Meguro staining, as earlier reported,[48,51] and correlated less with the ferritin map; therefore, our quantitative analysis was based on the Meguro staining for iron, only.

The $[Fe]_{ORS}$ metrics correlates with the Meguro staining ($\rho = 0.6$) and, although more moderately, with QSM ($\rho = 0.44$) and the ferritin staining ($\rho = 0.42$). $[Fe]_{ORS}$ also inversely correlates with the myelin staining ($\rho = -0.53$). No significant correlation was observed between $[Fe]_{ORS}$ and the R_2^* map. The association between QSM and R_2^* was not significant, probably due to the concurrent effects of iron and myelin to enhance transverse relaxation. The strongest correlation was found between the Meguro and the ferritin staining ($\rho = 0.7$), suggesting the high localization of iron within ferritin nanoparticles in the Alzheimer cortex. We anticipate that this result is rather consistent across cases.

The tissue block containing the striatum of the HD cases (Figure 4) (Supporting Information Figures S9 and S10) shows high R_2^* primarily in the putamen (PU), some connecting fibers of the internal capsule (IC), and a thin stripe of the atrophied caudate nucleus (CN). The susceptibility maps look heterogeneous but with an overall positive susceptibility in the putamen and CN. The IC shows a characteristic striped appearance of alternating positive and negative susceptibility. The $[Fe]_{ORS}$ map shows a localized increase of iron in the putamen and CN, and marginally on the white matter, depending on the case. The histological staining for ferritin, iron, and the $[Fe]_{ORS}$ map are largely opposite to the myelin-positive regions, which display negative susceptibility in the QSM map.

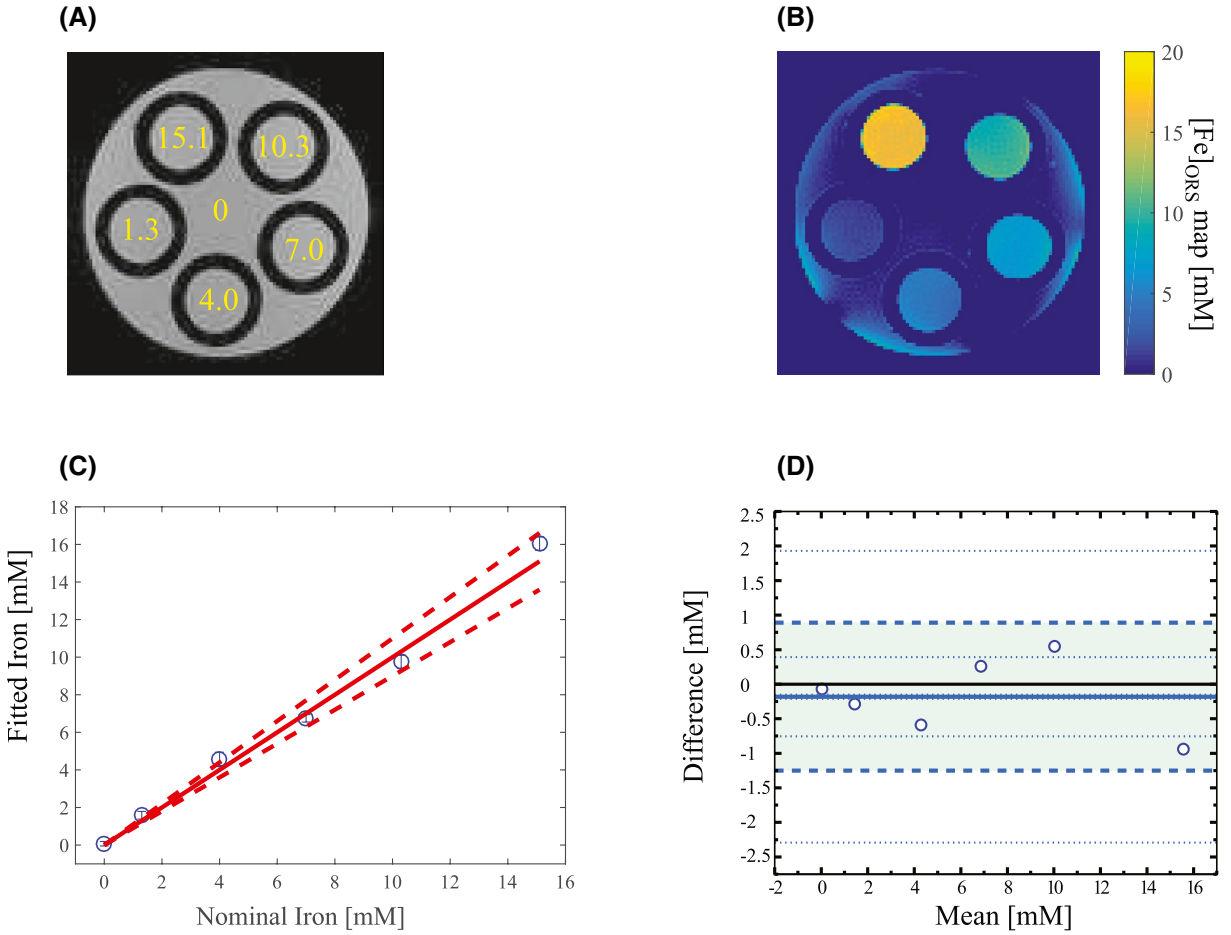

FIGURE 2 Validation on a ferritin phantom. Panel A shows the control image with the nominal iron concentration in mM per compartment. Panel B shows the mineral-iron map in mM, as obtained with the ORS sequence and the fitting method discussed above. The bright outer rim in the iron map is likely caused by B_1 inhomogeneities because a linear 8-leg birdcage coil with a high filling factor was employed. Panel C shows a comparison between the nominal iron concentration and the fitted one from the method discussed in this work. Blue data with error bars represent the mean and SD of the iron concentration in the ROI drawn in each sample compartment. The red solid line is the identity line and the dashed lines account for the spread in iron loading, as reported in literature for horse spleen ferritin from the same producer. Panel D is the Bland-Altman plot of the same data. The black solid line is the line of equality. The blue line is the bias. The dashed lines enclosing the green area are the limits of agreement. The dotted lines mark the 95% confidence intervals for each estimated statistical quantity. See Supporting Information Figures S1 and S2 for more details on the ferritin phantom. ROI, region of interest

The $[Fe]_{ORS}$ metrics correlates with the Meguro staining (ρ = 0.53-0.81) and QSM (ρ = 0.4-0.49) in 2 out of 3 cases, whereas no significant correlation is found with the ferritin staining in all the 3 examined cases. In 2 of the cases, $[Fe]_{ORS}$ correlates with R_2^* (ρ = 0.72-0.74), which in turns is uncorrelated with myelin, differently from the AD case, whereas it is correlated with the iron staining (ρ = 0.41-0.77). In 2 of the HD cases, QSM and R_2^* show a positive association with (ρ = 0.43-0.54). The strongest correlation was found between the Meguro and the ferritin staining (ρ = 0.45-0.85), similarly to the cortex of the Alzheimer subject. Both stainings show a negative association with myelin, in the first case.

Lastly, the tissue block obtained from the ACP patient (Figure 5) shows high R_2^* in the putamen, some connecting fibers of the IC, CN, and globus pallidus (R_2^*~0.3-0.6 ms^{-1}). The QSM map is relatively smooth in the white matter regions, whereas the gray matter is heterogeneous and presents a "patchy" appearance (also observed in the MGE images), which hinders quantitative analysis. The $[Fe]_{ORS}$ map on this tissue block shows diffuse iron across both white and gray matter structures, except for the superior part of the IC, where the ROR was drawn. The histological iron staining (Meguro) appears very intense across the whole slice, with a slightly higher intensity in the CN and the globus pallidus, which is also captured by the $[Fe]_{ORS}$ map. In contrast to the previous cases, the ACP ferritin staining was not used for the correlation analysis because it suffered from artifacts, likely due to formalin fixation. Additional histological results on all the tissue blocks are found in the Supporting Information (Figures S4-S8).

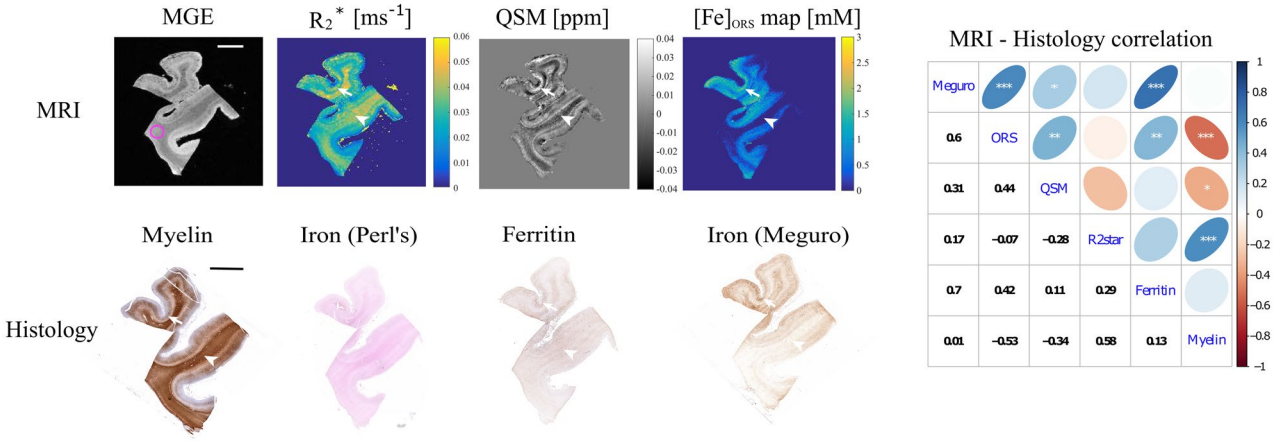

FIGURE 3 Comparison of the quantitative MRI and histological methods to assess tissue iron load on the Alzheimer tissue block: Top row: MRI R_2^*, QSM, and mineral-iron mapping. Bottom row: histological staining for myelin, iron (Perl's and Meguro), and ferritin (scalebar: 5 mm). The Meguro staining, and to a lesser extent the ferritin staining, appear weaker at the bottom of the tissue, likely due to prolonged formalin fixation. This is likely a real effect of the tissue because the same pattern is visible in the MRI metrics. The fourth echo of the MGE image is shown for anatomical reference. The pink circle in the MGE image encloses the ROR. The arrowheads point at the white matter, whereas the arrows point at the cortical sulcus. The panel on the right is a summary of the correlation analysis between all the contrasts and parameters here presented (see diagonal). The lower triangle reports the Pearson correlation coefficient, whereas the upper triangle is a visual representation of the correlation coefficient in the shape of an ellipse. The asterisks refer to the *P* value according to the convention: $P < .5$ (*), $P < .01$ (**), $P < .001$ (***). The intensity dropout at the top-right corner of the $[Fe]_{ORS}$ map is likely due to B_1 inhomogeneity. The reader is referred to the Supporting Information Figures S2 and S3 for more information on the data analysis

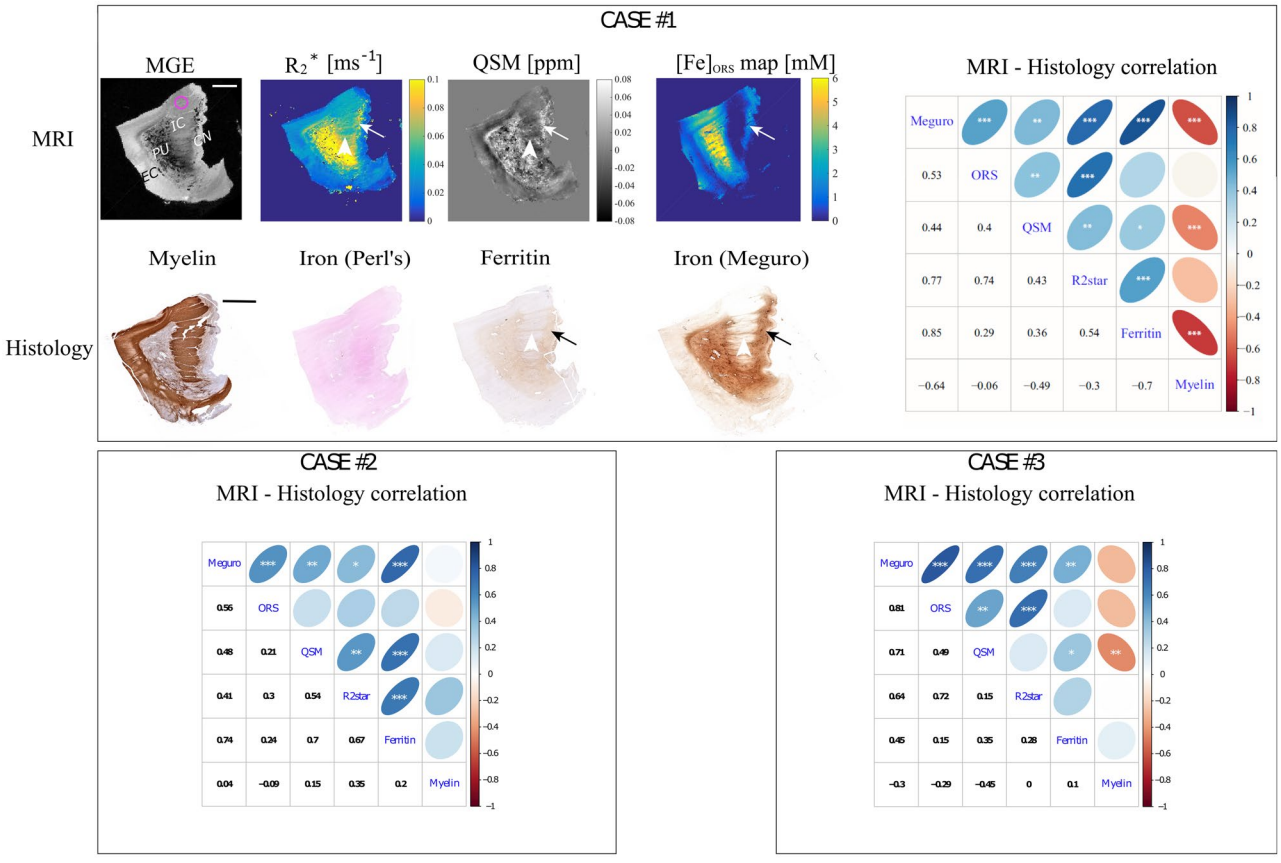

FIGURE 4 Comparison of the quantitative MRI and histological methods to assess tissue iron load in 3 Huntington tissue blocks (labels as above) (scalebar: 5 mm). The MGE image displays the third echo. The full-sized arrows point at the CN, whereas the arrowhead points at the gray-matter bridges between the PU and the CN. Please refer to Figure 3 for the details of the correlation matrix. The correlation matrices of 2 additional cases are shown in the bottom panels. The MRI and histology figures relative to these cases are shown in the Supporting Information Figures S9 and S10. CN, caudate nucleus; IC, internal capsule; MGE, multiple gradient echo; PU, putamen

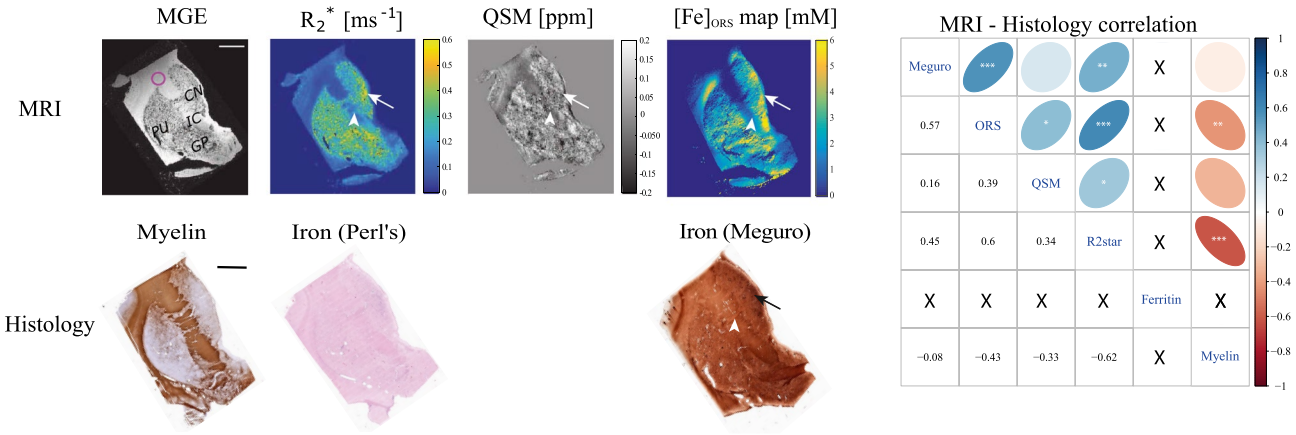

FIGURE 5 Comparison of the quantitative MRI and histological methods to assess tissue iron load on the aceruloplasminemia tissue block (labels as above) (scalebar: 5 mm). The MGE image displays the first echo. The full-sized arrows point at the CN, whereas the arrowhead points at the gray-matter bridges between the PU and the CN nucleus. Please refer to Figure 3 for the details of the correlation matrix. Note that the ferritin staining is not shown here (please refer to the Supporting Information Figure S8) due to the poor quality of the image, resulting from prolonged formalin fixation. GP, globus pallidus

The $[Fe]_{ORS}$ metrics shows a significant and positive correlation with the Meguro staining ($\rho = 0.57$), and the QSM map ($\rho = 0.39$), whereas it displays a negative association with myelin ($\rho = -0.43$). Also in this case, $[Fe]_{ORS}$ correlates with R_2^* ($\rho = 0.6$). QSM and R_2^* show a moderate mutual association ($\rho = 0.34$).

4 | DISCUSSION

In this work, we demonstrate how a method based on diffusion-mediated off-resonance saturation (ORS)[39] can detect mineral-iron from postmortem brain material of 1 AD patient, 3 HD patients, and 1 ACP patient. This method can be translated in vivo to evaluate tissue iron load and therapeutic efficacy on a pathophysiological level. Throughout this study, we have assumed that the mineral form of iron was ferritin-bound, that is, ferrihydrite. More than 80% of non-heme brain iron is stored within cells— in ferritin—and ferritin-bound iron is by far the most magnetic non-heme iron species in the brain.[19] We thus used the magnetization of ferritin to estimate the iron concentration. It is important to stress that there is an additional pool of iron forms[36] (way much less magnetic and/or abundant), which will possibly affect the ORS metric, although to a lesser degree. Nonetheless, the weak/absent correlation between the $[Fe]_{ORS}$ metric and the ferritin stain highlights the fact that the ORS method is primarily sensitive to iron rather than the ferritin protein, and that the magnetization of ferritin nanoparticles as well as the composition of the protein shell may vary in presence of pathology, as earlier studies have suggested.[16,52]

Water molecules diffusing around iron particles can be selectively excited by ORS pulses based on the correspondence between frequency offset and distance from the nanoparticle: the larger the frequency offset, the closer the protons are to the dipolar-field source. It has been shown that the positive contrast obtained by this method is distinct from, and can be observed also in the presence of, MT effects.[39] Although the ORS method was originally introduced to detect superparamagnetic iron-oxide nanoparticles, here we show that ORS can also be employed to assess the presence and the concentration of mineral-iron in the human postmortem brain by virtue of the super-paramagnetic properties of the protein and its high concentration across the brain. Our results on the agarose phantom show good agreement between nominal and fitted iron concentrations and support the use of the method for iron quantification.

The comparison between the parametric MRI maps acquired in this study shows some advantages of the ORS method over existing MR methods for tissue iron detection in postmortem tissue: 1) iron load appears primarily localized in specific brain regions (mainly the gray matter); 2) the white matter structures, which are highly myelinated, are characterized by low intensity in the $[Fe]_{ORS}$ maps, except for the ACP tissue where iron appears largely diffuse throughout the whole slice; and 3) the strength of the association between the $[Fe]_{ORS}$ maps and the iron staining is largely independent of the disease type and the brain region.

The appearance of the mineral-iron map in the tissue block obtained from the AD patient suggests that, when looking at the temporal lobe, iron preferentially accumulates in the cortical gray matter. This is in agreement with previous R_2^*[53,54] and QSM studies[55] reporting increased cortical iron levels in patients with AD or mild cognitive impairment, which was associated with AD pathological

hallmarks and an increased risk of cognitive decline. Magnetometry studies carried out on both sporadic and genetic types of AD have also found that ferrihydrite-iron is more abundant in the AD group than in age- and gender-matched healthy controls.[56,57]

Previous analytical studies have detected significant increase in the *total* iron content of the temporal lobe of AD patients with respect to controls.[58,59] However, the absolute iron concentrations ranged from ~30 μg/g[59] to 120 μg/g (wet weight)[60] because age, gender, disease state, and technique sensitivity can impact the measured iron values. The highest cortical mineral-iron concentrations detected in our tissue block were 1.37 ± 0.25 mM (mean ± SD), corresponding to 76.45 ± 13.95 μg/g, which is in agreement with the estimate of ferritin-bound iron by magnetometry in the AD temporal cortex[57] after correcting for dry weight mass-loss.

The mineral-iron map of the tissue block from the HD patient shows an increase of iron in the putamen and part of the atrophic CN. Alterations in brain iron metabolism with increased iron accumulation have been previously identified by MRI in the striatal nuclei of patients with HD.[26,61] Iron accumulation in these structures seems to occur early on during the disease process,[62] suggesting a key role of iron in the initiation and progression of the disease.[11] In fact, in vivo MRI studies at both 3 Tesla and 7 Tesla have shown that iron accumulation[63] is associated with tissue atrophy of basal ganglia structures and is already present in the premanifest phase of HD.[62,64,65] Our mean fitted iron concentration in the putamen, 4.66 ± 1.35 mM, equivalent to 260.0 ± 75.33 μg/g, agrees well with iron concentrations measured by inductively coupled mass spectrometry (~240-310 μg/g).[12]

Finally, the mineral-iron map of the ACP tissue block shows a very diffuse iron load, with mean iron values of 2.57 ± 1.45 mM, in the putamen, which is about 50% lower than found by our magnetometry study—and which quantified ferritin-iron in the same structure of the same patient.[66] This is likely due to the combination of very fast relaxation times and the lack of an appropriate ROR in the slice.

In contrast to AD and HD, iron accumulation in ACP is directly related to its genetic background and results from the absence of functioning ceruloplasmin.[13] The lack of ceruloplasmin-mediated oxidation of ferrous iron (Fe^{2+}) to ferric iron (Fe^{3+}) impairs iron efflux from astrocytes and leads to massive iron accumulation within these cells, whereas neurons that are mainly dependent on the supply of iron from astrocytes are probably iron-starved.[13,67] Although ferritin-bound iron appears to be by far the most abundant iron form in the aceruloplasminemia brain,[66,68,69] these observations are based on patients with end-stage aceruloplasminemia, and it remains unclear how the increase in either total iron levels, as suggested by previous R_2^*[13,70,71] and QSM studies,[70] or in the amount of ferritin-bound iron, is associated with the clinical course of the disease. In both the ACP case and 1 of the HD cases, it is noticeable that R_2^* appears, in a first instance, to be a better marker for iron than QSM, whereas the situation is clearly different in the AD case. It is important to note that the R_2^* enhancement can be influenced by multiple factors: for example, the different levels of iron across the different tissue samples but also the way that iron and myelin are spatially arranged/aggregated and their level of heterogeneity. It seems reasonable to conclude from this limited number of cases that at high iron concentrations, the iron level dominates the correlation; however, more in vitro and postmortem work will be needed to be able to build a quantitative model of the relative contribution of iron and myelin to R_2^*, QSM, or ORS contrasts.

Different MRI methods, in addition to those already mentioned, have been used to estimate the effect of ferritin nanoparticles on the MRI parameters. In fact, ferritin-bound iron has long been identified as the main source of iron-driving contrast, given the large abundance of the protein in the brain and its magnetic properties. The magnetic susceptibility of a single ferritin protein was estimated as $\chi = 520$ ppm for a fully loaded particle,[19] although this value might be an upper limit.[18,72]

Ferritin-iron displays a peculiar linear inverse dependence of T_2 with B_0 field,[73] a trend that is retained in brain tissue and is attributed to the "fingerprint" of iron stores. This characteristic is exploited by the field-dependent transverse relaxation rate increase metrics.[74]

A method based on direct saturation to sensitize image contrast due to iron load[75] has demonstrated a linear relation with the tissue iron content and an improved gray matter–white matter contrast with respect to T_2-weighted images. The ORS method here proposed differs in the acquisition protocol, with a much larger ORS frequency range being probed, as well as in the data postprocessing.

When inspecting the mineral-iron maps, some caveats should be considered. Firstly, our method assumes that the only source of contrast consists of ferrihydrite nanoparticles (i.e., inside ferritin). This is a simplification because ferrihydrite is also included in hemosiderin.[76] Also, magnetite/maghemite is located in the brain either outside or within ferritin.[16,77] Previous studies have shown that these additional minerals are approximately 3 orders of magnitude less abundant than mineral-iron.[56,57]

Secondly, we assumed that the iron loading of each ferritin protein was approximately equal to half of the maximum filling capacity of the homonymous protein, whereas a lower iron loading range (i.e. 1500-1850 iron ions within each ferritin protein) has been reported for AD brain tissue and controls.[78] However, because the

magnetization of the ferritin particle would not, or would only minimally, depend on the iron loading, this consideration does not significantly affect the total ferritin-iron concentrations reported here.

Moreover, the data in this study were acquired with a simple linear 8-leg birdcage coil with high filling factor, which makes the image prone to B_1-inhomogeneities. This may result in signal dropouts in the contrast maps and in the corresponding fitted $[Fe]_{ORS}$ maps (see for example, Figures 2 and 3). Future solutions could be to incorporate B_1 and B_0 correction in the analysis pipeline or to use a larger coil with slightly lower filling factor.

Additionally, the mineral-iron maps were obtained from contrast maps that were referenced to a region (ideally) without iron. Therefore, the iron concentrations here displayed cannot be considered as absolute. This is especially clear in the case of the ACP tissue block.

The comparison of the $[Fe]_{ORS}$ maps to the semi-quantitative[51] Meguro staining instead of a quantitative assessment of iron in the tissue is an obvious limitation of our study; therefore, the effect of potential confounders, specifically myelin fiber orientation, cannot be totally ruled out.

T_2 maps (not acquired in this study) can provide additional information on the degree of iron accumulation and, in combination with the T_2^* maps, could offer valuable information on the effective size of iron-rich compartments.[79]

Finally, although this study was intended to demonstrate the feasibility and value of the ORS method postmortem, we believe that in vivo translation is very important and could be challenging given that ORS requires the acquisition of multiple 2D images in order to derive the iron map, resulting in a relatively long scan time. It should therefore be noted that accommodating the sequence into an in vivo protocol, without any acceleration technique,[80–82] may well result in reduced spatial resolution or SNR compared to the postmortem results presented here.

Another important factor to consider when interpreting these results in terms of their significance for the in vivo case is the effect of formalin fixation. Although T_2 and T_2^* are known to be shortened by fixation,[83] this effect can be restored by washing the sample in phosphate-buffered solution for at least 12 h.[84] Because our tissue blocks were rehydrated for ~24 h prior to each scan session, the relaxation times are likely close to the situation prior to fixation.

A final difference with the in vivo case is the temperature: considering the Curie-Weiss-like change of the magnetization of ferritin at 7 T,[85] a maximum reduction of ~10% in the particle's equatorial field can be expected, with respect to the in vivo case.

5 | CONCLUSION

We adapted an ORS method[46,39] to quantify the mineral-iron pool in the postmortem brain tissue of 5 patients affected by neurological diseases associated with increased brain iron. This method can aid the interpretation of R_2^* and QSM maps, especially when these are confounded by reconstruction artifacts or the co-presence of iron and myelin. The accuracy of the mineral-iron map depends on the availability, within the tissue, of a region without (or with little) iron content with respect to the ROI. We foresee that this method will find use in the study of the progression of neurodegenerative diseases characterized by brain iron accumulation and the assessment of iron chelation therapy.

ACKNOWLEDGMENT

The authors are grateful to E. Suidgeest and E. Ercan for assistance in the lab and useful discussions.

ORCID

Lucia Bossoni https://orcid.org/0000-0003-3156-4696
Lydiane Hirschler https://orcid.org/0000-0003-2379-0861
Andrew Webb https://orcid.org/0000-0003-4045-9732

TWITTER

Lucia Bossoni @lucia_bossoni

REFERENCES

1. Hallgren B, Sourander P. The effect of age on the non-haemin iron in the human brain. *J Neurochem*. 1958;3:41-51.
2. Ward RJ, Zucca FA, Duyn JH, Crichton RR, Zecc L. The role of iron in brain ageing and neurodegenerative disorders. *Lancet Neurol*. 2014;13:1045-1060.
3. Zecca L, Youdim MBH, Riederer P, Connor JR, Crichton RR. Iron, brain ageing and neurodegenerative disorders. *Nat Rev Neurosci*. 2004;5:863-873.
4. Li K, Reichmann H. Role of iron in neurodegenerative diseases. *J Neural Transm*. 2016;123:389-399.
5. Daugherty AM, Raz N. Appraising the role of iron in brain aging and cognition: promises and limitations of MRI methods. *Neuropsychol Rev*. 2015;25:272-287.
6. Harman D. Aging: a theory based on free radical and radiation chemistry. *J Gerontol*. 1956;11:298-300.
7. Ashraf A, Clark M, So PW. The aging of iron man. *Front Aging Neurosci*. 2018;10:1-23.
8. Stockwell BR, Friedmann Angeli JP, Bayir H, et al. Ferroptosis: a regulated cell death nexus linking metabolism, redox biology, and disease. *Cell*. 2017;171:273-285.
9. Angeli JPF, Shah R, Pratt DA, Conrad M. Ferroptosis inhibition: mechanisms and opportunities. *Trends Pharmacol Sci*. 2017;38:489-498.
10. Ong W-Y, Farooqui AA. Iron, neuroinflammation, and Alzheimer's disease. *J Alzheimer's Dis*. 2005;8:183-200.
11. Rivera-Mancía S, Pérez-Neri I, Ríos C, Tristán-López L, Rivera-Espinosa L, Montes S. The transition metals copper

and iron in neurodegenerative diseases. *Chem Biol Interact*. 2010;186:184-199.
12. Rosas HD, Chen YI, Doros G, et al. Alterations in brain transition metals in Huntington disease: an evolving and intricate story. *Arch Neurol*. 2012;69:887-893.
13. Miyajima H. Aceruloplasminemia. *Neuropathology*. 2015;35: 83-90.
14. Finazzi D, Arosio P. Biology of ferritin in mammals: an update on iron storage, oxidative damage and neurodegeneration. *Arch Toxicol*. 2014;88:1787-1802.
15. Arosio P, Elia L, Poli M. Ferritin, cellular iron storage and regulation. *IUBMB Life*. 2017;69:414-422.
16. Quintana C, Gutiérrez L. Could a dysfunction of ferritin be a determinant factor in the aetiology of some neurodegenerative diseases? *Biochim Biophys Acta*. 2010;1800:770-782.
17. Schenck JF, Zimmerman EA. High-field magnetic resonance imaging of brain iron: birth of a biomarker? *NMR Biomed*. 2004;17:433-445.
18. Makhlouf SA, Parker FT, Berkowitz AE. Magnetic hysteresis anomalies in ferritin. *Phys Rev B*. 1997;55:R14717-R14720.
19. Schenck JF. Health and physiological effects of human exposure to whole-body four-Tesla magnetic fields during MRI. *Ann N Y Acad Sci*. 1992;649:285-301.
20. Salgado JC, Olivera-Nappa A, Gerdtzen ZP, et al. Mathematical modeling of the dynamic storage of iron in ferritin. *BMC Syst Biol*. 2010;4:147.
21. Kakhlon O, Gruenbaum Y, Cabantchik ZL. Repression of ferritin expression increases the labile iron pool, oxidative stress, and short-term growth of human erythroleukemia cells. *Blood*. 2001;97:2863-2871.
22. Ghassaban K, Liu S, Jiang C, Haacke EM. Quantifying iron content in magnetic resonance imaging. *Neuroimage*. 2019;187: 77-92.
23. Chavhan GB, Babyn PS, Thomas B, Shroff MM, Haacke EM. Principles, techniques, and applications of T2*-based MR imaging and its special applications. *Radiogr Educ Exhib*. 2009;29: 1433-1449.
24. Brass SD, Chen NK, Mulkern RV, Bakshi R. Magnetic resonance imaging of iron deposition in neurological disorders. *Top Magn Reson Imaging*. 2006;17:31-40.
25. Bartzokis G, Sultzer D, Mintz J, et al. In vivo evaluation of brain iron in Alzheimer's disease and normal subjects using MRI. *Biol Psychiatry*. 1994;35:480-487.
26. Bartzokis G, Lu PH, Tishler TA, et al. Myelin breakdown and iron changes in Huntington's disease: pathogenesis and treatment implications. *Neurochem Res*. 2007;32:1655-1664.
27. Raven EP, Lu PH, Tishler TA, Heydari P, Bartzokis G. Increased iron levels and decreased tissue integrity in hippocampus of Alzheimer's disease detected in vivo with magnetic resonance imaging. *J Alzheimer's Dis*. 2013;37:127-136.
28. Langkammer C, Krebs N, Goessler W, et al. Quantitative MR imaging of brain iron: a postmortem validation study. *Radiology*. 2010;257:455-462.
29. Haacke EM, Cheng NYC, House MJ, et al. Imaging iron stores in the brain using magnetic resonance imaging. *Magn Reson Imaging*. 2005;23:1-25.
30. Langkammer C, Schweser F, Krebs N, et al. Neuroimage quantitative susceptibility mapping (QSM) as a means to measure brain iron? A post mortem validation study. *Neuroimage*. 2012; 62:1593-1599.
31. Eskreis-Winkler S, Zhang Y, Zhang J, et al. The clinical utility of QSM: disease diagnosis, medical management, and surgical planning. *NMR Biomed*. 2017;30:e3668.
32. Hametner S, Endmayr V, Deistung A, et al. The influence of brain iron and myelin on magnetic susceptibility and effective transverse relaxation – a biochemical and histological validation study. *Neuroimage*. 2018;179:117-133.
33. Li T-Q, Yao B, van Gelderen P, et al. Characterization of T(2)* heterogeneity in human brain white matter. *Magn Reson Med*. 2009;62:1652-1657.
34. Stüber C, Morawski M, Schäfer A, et al. Myelin and iron concentration in the human brain: a quantitative study of MRI contrast. *Neuroimage*. 2014;93:95-106.
35. Wharton S, Bowtell R. Fiber orientation-dependent white matter contrast in gradient echo MRI. *Proc Natl Acad Sci USA*. 2012;109:18559-18564.
36. Möller HE, Bossoni L, Connor JR, et al. Iron, myelin, and the brain: neuroimaging meets neurobiology. *Trends Neurosci*. 2019;42:384-401.
37. Tanimoto A, Oshio K, Suematsu M, Pouliquen D, Stark DD. Relaxation effects of clustered particles. *J Magn Reson Imaging*. 2001;14:72-77.
38. Gossuin Y, Gillis P, Muller RN, Hocq A. Relaxation by clustered ferritin: a model for ferritin-induced relaxation in vivo. *NMR Biomed*. 2007;20:749-756.
39. Zurkiya O, Hu X. Off-resonance saturation as a means of generating contrast with superparamagnetic nanoparticles. *Magn Reson Med*. 2006;56:726-732.
40. Delangre S, Vuong QL, Henrard D, Po C, Gallez B, Gossuin Y. Bottom-up study of the MRI positive contrast created by the off-resonance saturation sequence. *J Magn Reson*. 2015;254:98-109.
41. Jian N, Dowle M, Horniblow RD, Tselepis C, Palmer RE. Morphology of the ferritin iron core by aberration corrected scanning transmission electron microscopy. *Nanotechnology*. 2016;27:46LT02.
42. Li W, Avram AV, Wu B, Xiao X, Liu C. Integrated Laplacian-based phase unwrapping and background phase removal for quantitative susceptibility mapping. *NMR Biomed*. 2014;27:219-227.
43. Li W, Wang N, Yu F, et al. A method for estimating and removing streaking artifacts in quantitative susceptibility mapping. *Neuroimage*. 2015;108:111-122.
44. van Zijl P, Yadav N. Chemical exchange saturation transfer (CEST): what is in a name and what isn't? *Magn Reson Med*. 2011;65:927-948.
45. Vuong QL, Berret JF, Fresnais J, Gossuin Y, Sandre O. A universal scaling law to predict the efficiency of magnetic nanoparticles as MRI T2-contrast agents. *Adv Healthc Mater*. 2012;1:502-512.
46. Delangre S, Vuong QL, Po C, Gallez B, Gossuin Y. Improvement of the off-resonance saturation, an MRI sequence for positive contrast with SPM particles: theoretical and experimental study. *J Magn Reson*. 2016;265:99-107.
47. Bernstein MA, Kevin F, King XJZ. *Handbook of MRI Pulse Sequences*. Elsevier Academic Press; 2004.
48. van Duijn S, Nabuurs RJA, van Duinen SG, Natté R. Comparison of histological techniques to visualize iron in paraffin-embedded brain tissue of patients with Alzheimer's disease. *J Histochem Cytochem*. 2013;61:785-792.
49. Altman DG, Bland JM. Measurement in medicine: the analysis of method comparison studies. *J R Stat Soc*. 2008;32:307-317.

50. Giavarina D. Understanding Bland Altman analysis. *Biochem Medica*. 2015;25:141-151.
51. Bulk M, Abdelmoula WM, Geut H, et al. Quantitative MRI and laser ablation-inductively coupled plasma-mass spectrometry imaging of iron in the frontal cortex of healthy controls and Alzheimer's disease patients. *Neuroimage*. 2020;215:116808.
52. Connor JR, Snyder BS, Arosio P, Loeffler DA, LeWitt P. A quantitative analysis of isoferritins in select regions of aged, Parkinsonian, and Alzheimer's diseased brains. *J Neurochem*. 1995;65:717-724.
53. Damulina A, Pirpamer L, Soellradl M, et al. Cross-sectional and longitudinal assessment of brain iron level in Alzheimer disease using 3-T MRI. *Radiology*. 2020;15:192541.
54. Bulk M, Kenkhuis B, Van Der Graaf LM, Goeman JJ, Natté R, Van Der Weerd L. Postmortem T2∗-weighted MRI imaging of cortical iron reflects severity of Alzheimer's disease. *J Alzheimer's Dis*. 2018;65:1125-1137.
55. van Bergen JMG, Li X, Hua J, et al. Colocalization of cerebral iron with amyloid beta in mild cognitive impairment. *Sci Rep*. 2016;6:35514.
56. van der Weerd L, Lefering A, Webb A, et al. Effects of Alzheimer's disease and formalin fixation on the different mineralised-iron forms in the human brain. *Sci Rep*. 2020;10:16440.
57. Bulk M, van der Weerd L, Breimer W, et al. Quantitative comparison of different iron forms in the temporal cortex of Alzheimer patients and control subjects. *Sci Rep*. 2018;8:6898.
58. Tao Y, Wang Y, Rogers JT, Wang F. Perturbed iron distribution in Alzheimer's disease serum, cerebrospinal fluid, and selected brain regions: a systematic review and meta-analysis. *J Alzheimer's Dis*. 2014;42:679-690.
59. House MJ, St. Pierre TG, McLean C. 1.4T study of proton magnetic relaxation rates, iron concentrations, and plaque burden in Alzheimer's disease and control postmortem brain tissue. *Magn Reson Med*. 2008;60:41-52.
60. Yu X, Du T, Song N, et al. Decreased iron levels in the temporal cortex in postmortem human brains with Parkinson disease. *Neurology*. 2013;80:492-495.
61. Bartzokis G, Cummings J, Perlman S, Hance DB, Mintz J. Increased basal ganglia iron levels in Huntington disease. *Arch Neurol*. 1999;56:569-574.
62. Domínguez DJF, Ng ACL, Poudel G, et al. Iron accumulation in the basal ganglia in Huntington's disease: cross-sectional data from the IMAGE-HD study. *J Neurol Neurosurg Psychiatry*. 2016;87:545-549.
63. Jurgens CK, Jasinschi R, Ekin A, et al. MRI T2 hypointensities in basal ganglia of premanifest Huntington's disease. *Plos Curr*. 2010;2:RNN1173.
64. Van Bergen JM, Hua J, Unschuld PG, et al. Quantitative susceptibility mapping suggests altered brain iron in premanifest Huntington's disease. *AJNR Am J Neuroradiol*. 2016;5:789-796.
65. Sánchez-Castañeda C, Squitieri F, Di Paola M, Dayan M, Petrollini M, Sabatini U. The role of iron in gray matter degeneration in Huntington's disease: a magnetic resonance imaging study. *Hum Brain Mapp*. 2015;36:50-66.
66. Vroegindeweij LHP, Bossoni L, Boon AJW, et al. Quantification of different iron forms in the aceruloplasminemia brain to explore iron-related neurodegeneration. *NeuroImage Clin*. 2021;30:102657.
67. Jeong SY, David S. Age-related changes in iron homeostasis and cell death in the cerebellum of ceruloplasmin-deficient mice. *J Neurosci*. 2006;26:9810-9819.
68. Kaneko K, Hineno A, Yoshida K, Ohara S, Morita H, Ikeda S-I. Extensive brain pathology in a patient with aceruloplasminemia with a prolonged duration of illness. *Hum Pathol*. 2012;43:451-456.
69. Kaneko K, Yoshida K, Arima K, et al. Astrocytic deformity and globular structures are characteristic of the brains of patients with aceruloplasminemia. *J Neuropathol Exp Neurol*. 2002;61:1069-1077.
70. Zhou L, Chen Y, Li Y, et al. Intracranial iron distribution and quantification in aceruloplasminemia: a case study. *Magn Reson Imaging*. 2020;70:29-35.
71. Shang H-F. Desferrioxamine treatment of aceruloplasminemia: long-term follow-up. *Mov Disord*. 2011;26:2131-2147.
72. Brooks RA, Vymazal J, Goldfarb RB, Bulte JWM, Aisen P. Relaxometry and magnetometry of ferritin. *Magn Reson Med*. 1998;40:227-235.
73. Brooks RA, Vymazal J, Bulte JW, Baumgarner CD, Tran V. Comparison of T2 relaxation in blood, brain, and ferritin. *J Magn Reson Imaging*. 1995;5:446-450.
74. Bartzokis G, Aravagiri M, Oldendorf WH, Mintz J, Marder SR. Field dependent transverse relaxation rate increase may be a specific measure of tissue iron stores. *Magn Reson Med*. 1993;29:459-464.
75. Smith SA, Bulte JWM, van Zijl PCM. Direct saturation MRI: theory and application to imaging brain iron. *Magn Reson Med*. 2009;62:384-393.
76. Duyn JH, Schenck J. Contributions to magnetic susceptibility of brain tissue. *NMR Biomed*. 2017;30:1-37.
77. Kirschvink JL, Kobayashi-Kirschvink A, Woodford BJ. Magnetite biomineralization in the human brain. *Proc Natl Acad Sci USA*. 1992;89:7683-7687.
78. Dedman DJ, Treffry A, Candy JM, et al. Iron and aluminium in relation to brain ferritin in normal individuals and Alzheimer's-disease and chronic renal-dialysis patients. *Biochem J*. 1992;287:509-514.
79. Lee H, Baek SY, Chun SY, Lee JH, Cho HJ. Specific visualization of neuromelanin-iron complex and ferric iron in the human post-mortem substantia nigra using MR relaxometry at 7T. *Neuroimage*. 2018;172:874-885.
80. Lustig M, Donoho D, Pauly JM. Sparse MRI: the application of compressed sensing for rapid MR imaging. *Magn Reson Med*. 2007;58:1182-1195.
81. Pruessmann KP, Weiger M, Scheidegger MB, Boesiger P. SENSE: sensitivity encoding for fast MRI. *Magn Reson Med*. 1999;42:952-962.
82. McGibney G, Smith MR, Nichols ST, Crawley A. Quantitative evaluation of several partial Fourier reconstruction algorithms used in MRI. *Magn Reson Med*. 1993;30:51-59.
83. Birkl C, Langkammer C, Golob-Schwarzl N, et al. Effects of formalin fixation and temperature on MR relaxation times in the human brain. *NMR Biomed*. 2016;29:458-465.
84. Shepherd TM, Thelwall PE, Stanisz GJ, Blackband SJ. Aldehyde fixative solutions alter the water relaxation and diffusion properties of nervous tissue. *Magn Reson Med*. 2009;62:26-34.
85. Silva NJO, Millán A, Palacio F, et al. Temperature dependence of antiferromagnetic susceptibility in ferritin. *Phys Rev B*. 2009;79:104405.

SUPPORTING INFORMATION

Additional supporting information may be found in the online version of the article at the publisher's website.

FIGURE S1 R_2^* map of the ferritin-agarose phantom used as a reference in this study. These data were acquired with an MGE sequence with six echoes and the following parameters: $TE_1 = 5$ ms, $\Delta TE = 2.5$ ms, TR = 40 ms, 0.3 mm^3 resolution, NA = 5, FA = 8°. Total scan time 36 m 23 s

FIGURE S2 Illustration of the quality of the fit and fitting parameters for the three tissue blocks and the phantom. See Equation (2) of the main manuscript for the description of the parameters

FIGURE S3 Myelin (PLP) stain of the AD (A), HD (B) and ACP (C) cases with overlayed oval ROIs used for the MRI-histological correlation analysis (yellow circles). Regions close to or corresponding with the ROR are excluded

FIGURE S4 Histopathology on the AD tissue block. Close-up on the gyrus. Scalebar on the close-up is 1 mm

FIGURE S5 Histopathology on the HD tissue block. Close-up on putamen, internal capsule, and caudate nucleus. Scalebar on the close-up is 1 mm

FIGURE S6 Histopathology on the ACP tissue block. Close-up on the internal capsule, caudate nucleus, and part of the putamen. Scalebar on the close-up is 1 mm

FIGURE S7 Illustration of the iron accumulation in aceruloplasminemia brain. Panels A and C show the modified Meguro staining on the whole tissue slice. Panel A was obtained on a 20 μm slice and a protocol optimized for the slice thickness. Panel C was obtained on an adjacent slice of 20 μm, but with shorter incubation times (the protocol was optimized for a 5 μm protocol slides). Panel B and D are close-ups on the region of interest in the putamen (blue square). The images illustrate the exceptional degree of iron accumulation in ACP. Scale bar is 50 μm in B and D, and 5 mm in A and C

FIGURE S8 Illustration of the ferritin histological stain in aceruloplasminemia. The faint stain is an effect of the long formalin fixation. Scalebar: 5 mm

FIGURE S9 Details of the MRI and histology of the second HD case (striatum) displayed in Figure 4 of the main article. The arrow highlights the iron-rich caudate nucleus. The MGE shows the first echo. Scalebar is 5 mm. Labels are according to the definitions of the main article. The ROIs used for the correlation analysis are shown in the bottom-right panel. The ROR was drawn in the internal capsule, as in case #1 (see Figure 4)

FIGURE S10 Details of the MRI and histology of the third HD case (striatum) displayed in Figure 4 of the main article. The MGE shows the first echo. Scalebar is 5 mm. Labels are according to the definitions of the main article. The ROIs used for the correlation analysis are shown in the bottom-right panel. The ROR was drawn in the internal capsule, as in case #1 (see Figure 4)

How to cite this article: Bossoni L, Hegeman-Kleinn I, van Duinen SG, et al. Off-resonance saturation as an MRI method to quantify mineral-iron in the post-mortem brain. *Magn Reson Med*. 2022;87:1276–1288. doi:10.1002/mrm.29041